LETTERS
https://doi.org/10.1038/s41550-019-0791-2

nature astronomy

Multi-filament gas inflows fuelling young star-forming galaxies

D. Christopher Martin[1*], Donal O'Sullivan[1], Mateusz Matuszewski[1], Erika Hamden[1], Avishai Dekel[2], Sharon Lapiner[2], Patrick Morrissey[1], James D. Neill[1], Sebastiano Cantalupo[3], Jason Xavier Prochaska[4,5], Charles Steidel[1], Ryan Trainor[6], Anna Moore[7], Daniel Ceverino[8], Joel Primack[9] and Luca Rizzi[10]

Theory suggests that there are two primary modes of accretion through which dark-matter halos acquire the gas to form and fuel galaxies: hot- and cold-flow accretion. In cold-flow accretion, gas streams along cosmic web filaments to the centre of the halo, allowing for the efficient delivery of star-forming fuel. Recently, two quasar-illuminated H I Lyman α (Lyα)-emitting objects were reported to have properties of cold, rotating structures[1,2]. However, the spatial and spectral resolution available was insufficient to constrain the radial flows associated with connecting filaments. With the Keck Cosmic Web Imager (KCWI)[3], we now have eight times the spatial resolution, permitting the detection of these inspiralling flows. To detect these inflows, we introduce a suite of models that incorporate zonal radial flows, demonstrate their performance on a numerical simulation that exhibits cold-flow accretion, and show that they are an excellent match to KCWI velocity maps of two Lyα emitters observed around high-redshift quasars. These multi-filament inflow models kinematically isolate zones of radial inflow that correspond to extended filamentary emission. The derived gas flux and inflow path is sufficient to fuel the inferred central galaxy star-formation rate and angular momentum. Thus, our kinematic emission maps provide strong evidence that the inflow of gas from the cosmic web is building galaxies at the peak of star formation.

Theory predicts that the inflowing gas in cold streams gains angular momentum prior to entering the halo virial radius by tidal torques from the cosmic web[4–7]. Thus, gas is delivered with large angular momentum, producing a rotating and largely coplanar structure[4–7]. Large rotating nebulae are now being detected in Lyα emission[1,2,8], as are possible inflows[9]. At the same time the gas travels inward, necessitating a radial component to the flow. Because the gas is flowing in from discrete filaments, the spiral inflow is roughly organized into azimuthal zones associated with each filament.

A simple disk rotation model was adequate to describe the data obtained with the Palomar Cosmic Web Imager (PCWI) in prior work.[1,2] The recently commissioned Keck Cosmic Web Imager (KCWI)[3] provides a factor-of-eight spatial resolution gain (in number of pixels), and a factor-of-ten increase in sensitivity, which allows precision velocities to be measured at this much finer spatial scale. This improved capability allows us to probe higher-order components in the velocity structures of newly forming galaxies.

We require a quantitative framework in which to detect and characterize these higher-spatial-resolution components. We first describe this framework and how we have verified its efficacy by applying it to a mock data cube from a simulated galaxy that is exhibiting cold filamentary inflow. In a hierarchical decomposition of the velocity structure in a newly forming galaxy, one might expect to find at least three levels: simple rotation, radially and azimuthally varying components corresponding to the influence of inflowing filaments, and higher-order effects corresponding to complex gas dynamics on smaller scales (see figure 20 in ref. [4]).

We employ a series of four increasingly complex models: (1) simple Keplerian rotation in an NFW (Navarro–Frenk–White)[10] halo; (2) rotation plus a linearly varying radial component; (3) rotation with a radial component that varies both radially and azimuthally; and (4) rotation with both radial and azimuthal components both being azimuthally modulated. We test these models on a simulated protogalaxy, and then apply them to two Lyα-emitting objects observed with KCWI. We display the simulated galaxy side-by-side with the two observed objects in Fig. 2 and in the model fitting in Figs. 3, 4, in order to compare how the addition of multi-filament inflow (MFI) models improves the fit and isolates radial inflow zones in the model and in the two observed objects.

Model 1 takes the dark-matter halo mass, concentration, disk inclination and position angle as free parameters. Model 2 adds a radial velocity component, proportional to radius. Model 3 allows this radial component to vary with azimuth, with an azimuthal modal decomposition of the radial velocity profile. The azimuthal variation has three modes. Model 3a has one cycle per revolution, with independently determined phase and amplitude. A spiral phase variation with radius can also be added. Model 3b is the sum of a one- and two-cycle component, each providing two free parameters (plus the single spiral slope). Model 3c adds a three-cycle component to Model 3b. In Model 4 we allow the azimuthal profile to deviate from the NFW rotation model with a correction sharing the same spatial profile as the radial component.

These models are motivated by analysis of a simulated protogalaxy, VELA07[4,11,12]. Examination of the radial velocity profiles in the simulated protogalaxy shows azimuthally coherent zones apparently driven by the cold inflow filaments (Fig. 1). Radial flows

[1]Cahill Center for Astrophysics, California Institute of Technology, Pasadena, CA, USA. [2]Racah Institute of Physics, The Hebrew University of Jerusalem, Jerusalem, Israel. [3]Institute for Astronomy, ETH Zurich, Zurich, Switzerland. [4]Department of Astronomy and Astrophysics, University of California, Santa Cruz, CA, USA. [5]University of California Observatories, Lick Observatory, Santa Cruz, USA. [6]Department of Astronomy, University of California, Berkeley, Berkeley, CA, USA. [7]Research School of Astronomy and Astrophysics, The Australian National University, Canberra, Australian Capital Territory, Australia. [8]Universitat Heidelberg, Zentrum fur Astronomie, Institut fur Theoretische Astrophysik, Heidelberg, Germany. [9]Department of Physics, University of California, Santa Cruz, CA, USA. [10]W. M. Keck Observatory, Waimea, HI, USA. *e-mail: martinc@caltech.edu

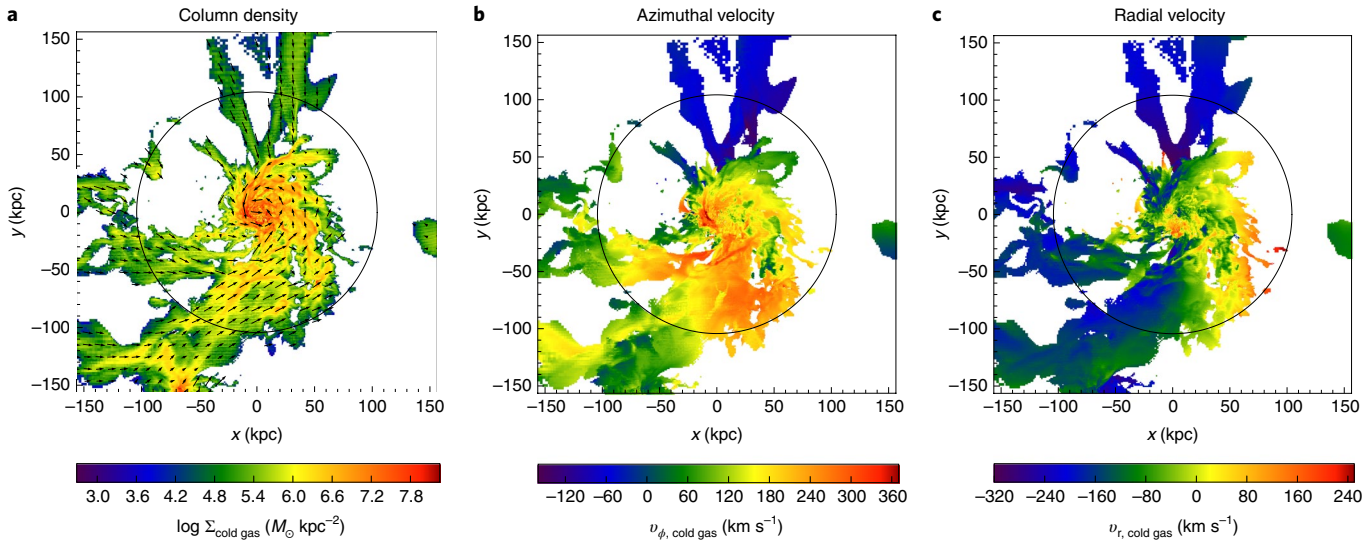

Fig. 1 | Surface density and velocity maps of VELA07 simulation in face-on projection. a, Column density, given on a logarithmic scale in units of $M_{\odot}$ per square kiloparsec. Arrows give local gas velocity magnitude and direction in the plane of the image. Circles in all panels are one virial radius. **b**, Colour value gives azimuthal gas velocity, with positive values corresponding to the anticlockwise direction. **c**, Colour value gives radial gas velocity, with negative values corresponding to inflow. All maps are 300 pkpc (proper kiloparsec) by 300 pkpc.

show both inflow and outflow variations, with inflow dominating over the full extent of the object but outflow regions on opposite sides where gas overshoots prior to circularizing. Large-scale features show a rough azimuthal modulation. On average, the radial velocity increases linearly with radius (see Supplementary Fig. 1).

Three data cubes were generated with orthogonal viewing directions, and mean intensity-weighted velocity and velocity dispersion maps generated using a velocity window that isolates the emitting region. The resulting simulated maps are given in Fig. 2a for one line of sight.

For each perspective, we fitted the MFI models to the simulation two-dimensional velocity profile. Derived physical parameters (Supplementary Table 4) are consistent with those of the simulation. For Model 3a(i), we derive a halo mass of $\log M_{\rm halo} = 11.9^{+0.2}_{-0.1}$, (simulation halo mass $\log M_{\rm halo} = 11.95$) and infer a mass-weighted radial flux within 50 kpc of $-24^{+6}_{-11} M_{\odot}\ {\rm yr}^{-1}$ (actual flux $-24 M_{\odot}\ {\rm yr}^{-1}$). The derived radial inflow direction corresponds to one of the major inflow filaments in the simulated protogalaxy. A prominent feature of the velocity maps (Fig. 3) is a distortion of the classical disk 'spider diagram' such that the velocity contours run orthogonally to their baseline directions wherever radial flow is strong.

We find that Model 1 is an adequate fit to the simulated galaxy velocity field, and that each successively more complex model invoking radial flow provides a better fit (Fig. 3, Fig. 4a, Supplementary Figs. 2, 3, Supplementary Table 4). This is quantified using the Akaike Information Criterion (AIC)[13], which appropriately penalizes free parameters, and is minimized for the best model. There is a large reduction in χ^2 and AIC moving from Model 2 to Model 3a(i) for each viewing direction. Although there are three filaments in the VELA07 simulation, the one in the lower left corner of Fig. 1a dominates because of its large column density and width. This filament is correctly detected by the MFI formalism and appears in Supplementary Fig. 2. The halo mass and mass inflow rate are also correctly derived. Similar results are obtained with two other simulated galaxies. We conclude that the MFI model can detect filamentary radial inflow in the gas velocity field of a forming galaxy. We provide a modified set of criteria for identifying a protogalaxy exhibiting MFI, extending our protogalactic disk criteria[2].

We now turn to the KCWI observations. We observed two quasar (QSO) fields with KCWI; UM287 and QSO B1009+2956. UM287 is a binary QSO field with clear and extended filamentary emission[14] in which observations with PCWI revealed an extended, rotating protodisk[1]. QSO B1009+2956 (CSO38) is a field in which extended emission was initially detected via narrow-band imaging[15,16] and subsequently followed up with PCWI. The Lyα emitters are extended blobs 80 pkpc and >120 pkpc in size for CSO38 and UM287 respectively, each showing a pronounced velocity shear and separated from the QSO by a projected 50–120 pkpc.

The emitting region near CSO38 (CSO38B) shows a central concentration as well as three filamentary extensions (Fig. 2, Supplementary Fig. 4), in two cases with low velocity dispersion, consistent with inflowing filaments[1,2,17,18]. The mean velocity displays a velocity shear of about 350 km s^{-1} coinciding with the central concentration, and the object meets all the criteria set out for a rotating structure with MFI components (Methods, Supplementary Table 2). There are continuum objects, two of which are galaxies near the redshift of the nebula.

Figure 2 shows the intensity, velocity and velocity dispersion maps for UM287. There is a large, lower-level-emission region and a bright extended region somewhat off-centre from the overall emission. There is velocity shear over the larger region and over the bright central region. The brightest emission comes from source C', which also has a very red velocity. There are some faint continuum sources but no continuum counterpart to the entire nebula. The Lyα emission from these sources may be enhanced by the presence of star formation. The observed properties of this object also compare favourably with the MFI criteria (Supplementary Table 2).

For CSO38B we find that Model 1 is an adequate fit to the data, and that each successively more complex model invoking radial flow provides a better fit, with the exception of Model 3c(i) (Fig. 3, Supplementary Fig. 2 and Supplementary Tables 5 and 7). There is a large reduction in χ^2 and AIC moving from Model 2 to Model 3a(i). The formal probability that Model 2 is a better representation of the data than Model 3a(i) is $<10^{-23}$, and that Model 1 is a better representation is $<10^{-32}$. For Model 3a(i) we derive a halo mass of $\log M_{\rm halo} = 11.25^{+0.11}_{-0.16}$, a mode-1 velocity amplitude of $v_{\rm r1} = -318^{+38}_{-27}$

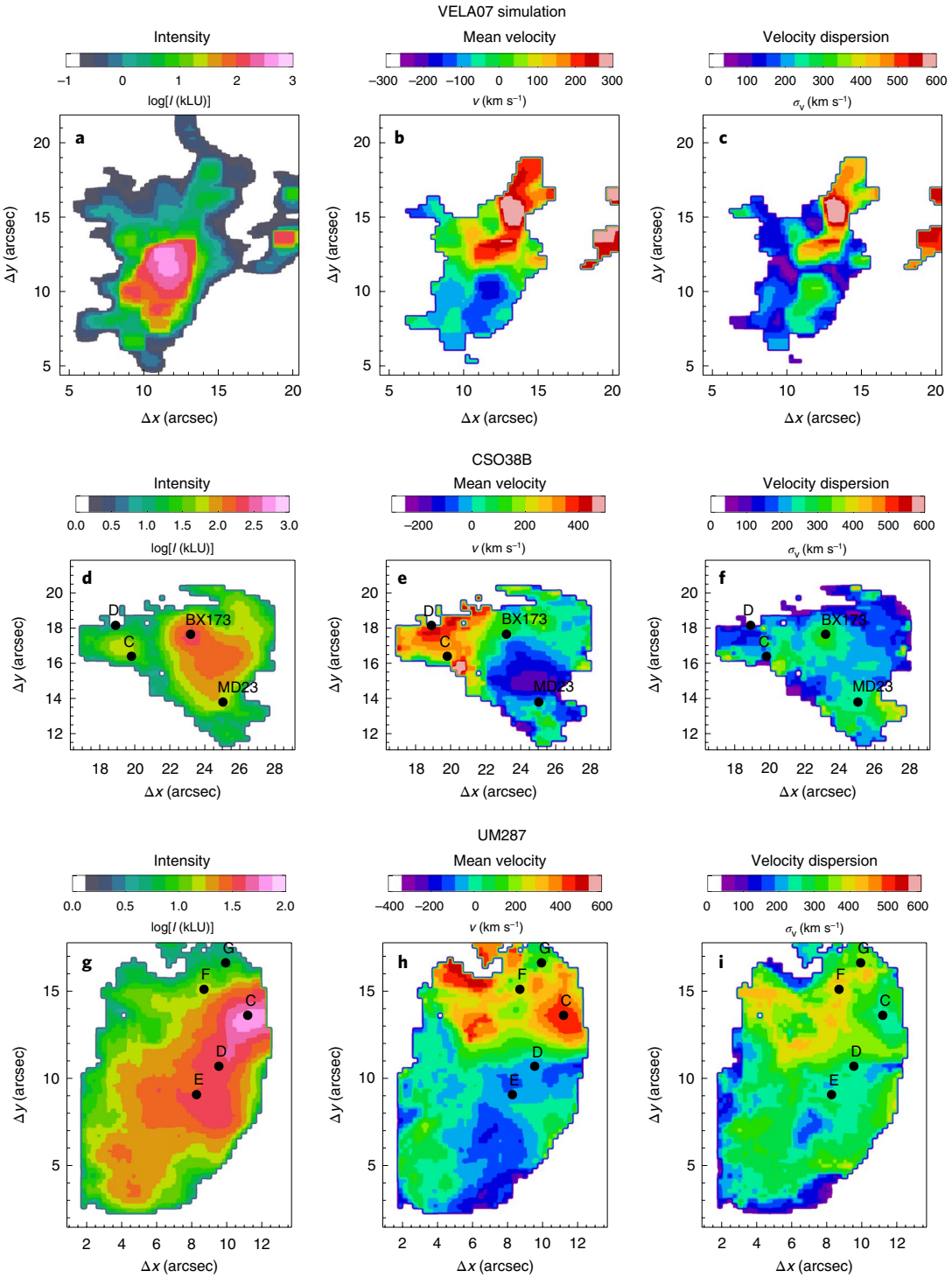

Fig. 2 | Narrow-band image, mean velocity map and velocity dispersion maps simulation and data. a–c, VELA07 simulation. **a**, Simulated narrow-band Lyα intensity map for the VELA07 simulation (in kLU, 1 LU = 1 photon $s^{-1} cm^{-2} sr^{-1}$). **b**, Mean (intensity-weighted) velocity for the VELA07 simulation. **c**, Velocity dispersion (intensity-weighted) for the VELA07 simulation. **d–f**, CSO38B. **d**, Narrow-band Lyα intensity map for CSO38B (in kLU). **e**, Mean (intensity-weighted) velocity for CSO38B. **f**, Velocity dispersion (intensity-weighted) for CSO38B. Continuum objects in the field also shown in this and in panels **g** and **h**. See Methods for discussion of continuum object properties. **g–i**, UM287. **g**, Narrow-band Lyα intensity map for UM287 (in kLU). **h**, Mean (intensity-weighted) velocity for UM287. **i**, Velocity dispersion (intensity-weighted) for UM287.

(an 8σ detection of the MFI radial mode), and a mass-weighted radial flux of $-39^{+6}_{-4} M_{\odot}\ yr^{-1}$ (a 6.5σ detection of radial inflow). The direction of radial inflow is along one of the extensions (Fig. 4; Supplementary Fig. 5). Halo concentration is not well constrained, and during fitting it is limited to the range $0 < \log c < 1$. The galaxy at the kinematic and intensity centre has a measured star-formation rate of $17 M_{\odot}\ yr^{-1}$. The gas inflow has the direction and magnitude to fuel this ongoing star formation and supply baryonic angular momentum in the same direction as the rotating component. We note that a model with only radial flow is excluded, since the

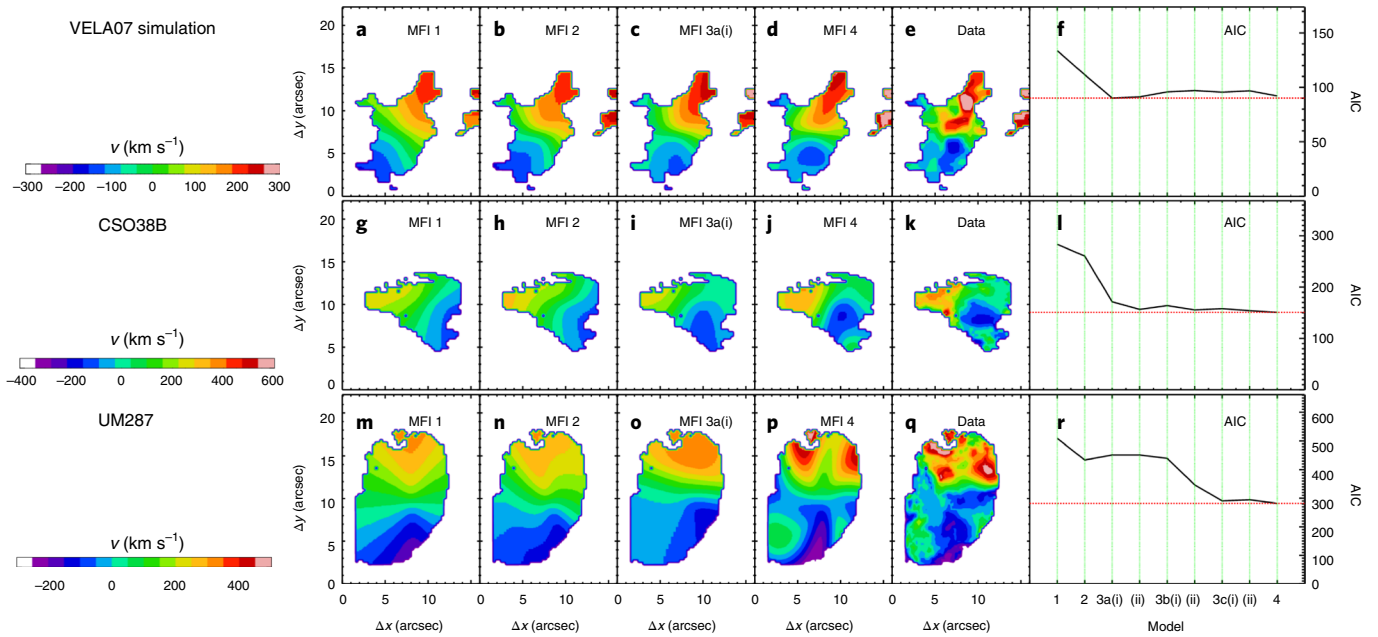

Fig. 3 | Velocity maps simulation and data compared to MFI models. a–f, VELA07 simulation. **a**, MFI Model 1 velocity map. **b**, MFI Model 2, **c**, MFI Model 3a(i). **d**, MFI Model 4 (Models 3a(ii), 3b and 3c not shown). **e**, Simulated VELA07 velocity map (as in Fig. 2b). **f**, AIC versus MFI model. The red dashed horizontal line shows minimum AIC (Model 3a(i)). **g–l**, CSO38B. **g**, MFI Model 1 velocity map. **h**, MFI Model 2. **i**, MFI Model 3a(i). **j**, MFI Model 4 (Models 3a(ii), 3b and 3c not shown). **k**, CSO38B velocity map (as in Fig. 2e). **l**, AIC versus MFI model. The red dashed horizontal line shows minimum AIC (Model 4). **m–r**, UM287. **m**, MFI Model 1 velocity map. **n**, MFI Model 2. **o**, MFI Model 3a(i). **p**, MFI Model 4. **q**, UM287 velocity map (as in Fig. 2h). **r**, AIC versus MFI model. The red dashed horizontal line shows minimum AIC (Model 4).

rotating component parameterized by the halo mass is required for a good fit. Alternative models are discussed in the Methods.

For UM287 we see a successive reduction in χ^2 and AIC for each model. Model 1 gives consistent results with the PCWI data and modelling: best-fit parameters for KCWI are halo mass $\log M_{\rm halo} = 12.7 \pm 0.05$, inclination $i = 65°$, baryon mass $\log M_{\rm baryon} = 11.2$, and for PCWI are $\log M_{\rm halo} = 13.1 \pm 0.6$, $i = 70°$, and $\log M_{\rm baryon} = 11.2$ The reduction going from Model 2 to Model 3 is not as large as for CSO38B and the VELA07 simulation. However, there is a pronounced fit improvement when the third mode is added to Model 3 (Model 3c(i) with AIC = 432) and to Model 4 (with AIC = 351). The formal probability that Model 3b(ii) is a better representation than Model 3c(i) is $<3 \times 10^{-17}$, and that Model 1 is a better representation is $<5 \times 10^{-73}$. Even the notional intensity model shows some agreement with the intensity map, suggesting that the morphology of the brightest emission is produced by filamentary inflow. The final velocity residual is comparable to CSO38B ($\sigma_v = 72$ km s^{-1}). The mode-3 component has a velocity amplitude $v_{r3} = 1,050^{+61}_{-133}$, an 8σ detection of this component. Inferred physical parameters for Model 4 suggest a higher-mass halo, with $\log M_{\rm halo} = 12.69^{+0.04}_{-0.16}$ consistent with the larger size of the object. Object C coincides with a positive radial flow consistent with an outflow produced by a starburst or active galactic nucleus. The mass-weighted radial flux of $-26^{+4}_{-7}\ M_\odot\ {\rm yr}^{-1}$, a 6.5σ detection of inflow, is comparable to the star-formation rate inferred for sources D and E[1], and the radial inflow direction is along the major filament[1,14] (Fig. 4, Supplementary Fig. 6, Supplementary Tables 6, 7). Again, the inflow supplies baryonic angular momentum consistent with that of the rotating component.

The excellent fit of MFI models with the VELA07 simulation demonstrates that cold spiral inflow can be detected in kinematic Lyα emission line maps. As we discuss in Methods, radiative transfer effects, galactic winds, tidal interactions in the gas–galaxy systems, and the selection of QSO-illuminated objects do not much affect the conclusions, and the cold inflow scenario incorporates both smooth accretion and clumpy satellite accretion. One azimuthal mode provides a good fit to the simulation and CSO38B, consistent with a single filament dominating the inflow. The presence of three modes in UM287 is consistent with the observation that two to three prominent filaments tend to appear in cold accretion inflow models[19] and may be a result of higher mass, larger size (and correspondingly improved resolution of the complex velocity field), different geometry or other factors. Theory suggests that this halo mass is a regime in which cold accretion flows penetrate a hot virialized halo, which could help to explain the increased complexity of the flow[20]. The MFI components and radial influx are detected even when we assume that the turbulent velocity field in the objects determines the root-mean-square velocity error and AIC. The data have a high signal-to-noise ratio and Poisson noise does not affect the detection of the MFI components. It is the much higher spatial resolution of the KCWI data that has allowed us to detect the MFI components. In both objects the detected inflow connects an extended filament with a flow direction and magnitude consistent with the star-formation rate in the central galaxy and the angular momentum of the rotating gas component. Thus these observations and MFI modelling using detailed emission-line velocity maps demonstrate that cold inspiral accretion is a dominant mode of gas delivery for star-forming galaxies at high redshift.

It is important to note that we are not attempting here a thorough quantitative comparison of simulations and observations. The one simulation addressed here, as an example, serves as an indicator of the likely qualitative consistency between the parametric model as applied to the observations and robust features extracted from cosmological simulations. It is an important step in interpreting the model and observational results in terms of a picture of galaxy formation within the cosmic web that emerges from both simulations and theory.

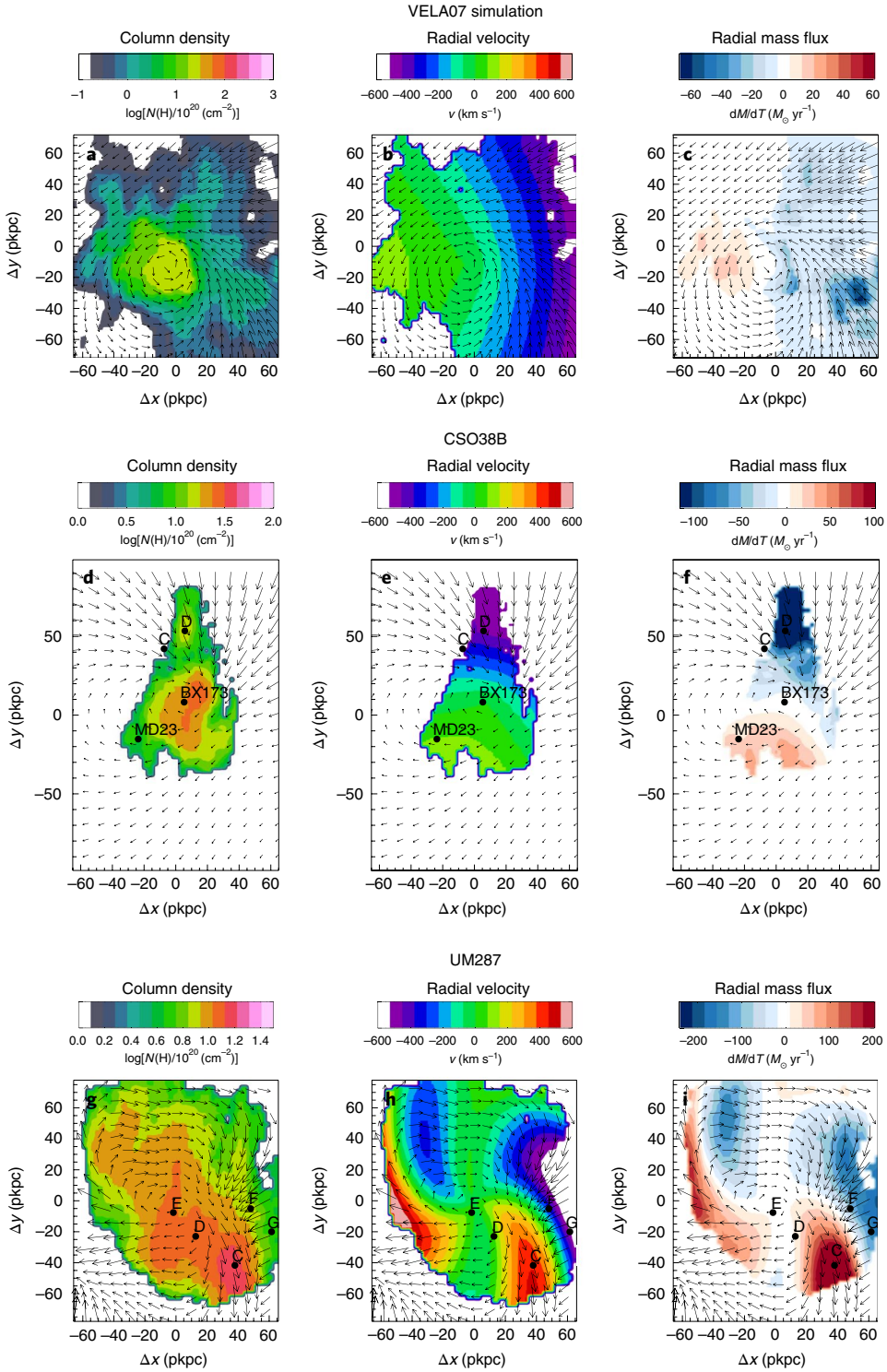

Fig. 4 | Face-on reconstruction of column density, radial velocity and radial mass flux for simulated and observed objects. All plots show the inferred total velocity field with arrows. The VELA07 simulation and CSO38B use Model 3a(i), and UM287 uses Model 4. **a**, VELA07 simulation column number density (*N*) for Model 3a(i). **b**, VELA07 simulation radial velocity component from Model 3a(i). **c**, VELA07 simulation radial mass flux. **d**, CSO38B column density. **e**, CSO38B radial velocity component from Model 3a(i). **f**, CSO38B radial mass flux. **g**, UM287 nebula column density. **h**, UM287 nebula radial velocity component. **i**, UM287 radial mass flux. In all cases the mass flux amplitude plotted is $2\pi r d\dot{M}/d\phi$ (see Methods). The total mass flux through radius *r* is the average of the plotted flux on the circle of radius *r*. Continuum objects have been remapped to the face-on position and superposed.

Methods

Observations. KCWI is an integral field spectrograph designed to observe objects of extremely low surface brightness[3], mounted at the Nasmyth focus of Keck II. In a 1-h observation, with the medium image slicer and BM, the medium-resolution blue grating, the 5σ limiting emission line flux is 6×10^{-18} erg cm^{-2} s^{-1} arcsec^{-2} in a $1''\times1''$ spatial bin, assuming a linewidth of 4 Å.

A summary of the observations, along with target information, is presented in Supplementary Table 1. KCWI observations of CSO38 were made with the

large image slicer and medium resolution grating ($\Delta\theta \approx 0.7''$, $\Delta\lambda \approx 2.5$ Å, FOV $= 16'' \times 20''$) to a limiting sensitivity of 3×10^{-18} erg cm^{-2} s^{-1} arcsec^{-2} ($1''\times1''$) in a 4-Å line. KCWI observation of UM287 were made with the medium image slicer and medium-resolution grating ($\Delta\theta \approx 0.6''$, $\Delta\lambda \approx 1$ Å, FOV $= 33''\times20''$) to a limiting sensitivity of 3×10^{-18} erg cm^{-2} s^{-1} arcsec^{-2} ($1''\times1''$) in a 4-Å line. We discuss the methodology and details of our observations and data analysis extensively in previous work[1,2,17,18]. The KCWI data reduction pipeline produces three-dimensional flux cubes (α, δ, λ) which we then adaptively smooth to optimally extract emission on different spatial scales.

For the UM287 observation, separate sky images have been interleaved between the science target observations and spatially smoothed to reduce the sky noise introduced by subtraction. The nod-and-shuffle mode provides exquisite sky subtraction, but we have found for these brighter Lyα objects (typical intensities 30,100 kLU) that the throughput of KCWI is high enough and the sky background at Keck is low enough that sky subtraction of <0.5% is sufficient for excellent detections (corresponding to an additional error of about 1 kLU). A three-point dithering pattern of –0.5, 0 and +0.5 slice widths perpendicular to the slices is used to obtain better point-spread-function sampling in the co-added cube.

Data analysis. The KCWI pipeline is open source and can be downloaded from https://github.com/kcwidev/kderp. It is written in IDL and consists of eight stages. Raw images are bias and overscan subtracted, gain-corrected, trimmed and cosmic-ray removed. Dark subtraction and scatter light removal is performed. Calibration images taken with the same settings are used to define the geometric transformations to map each pixel in the two-dimensional image to slice, position and wavelength position. Flat-field and illumination corrections are performed. Sky subtractions can also be performed, either via nod-and-shuffle, a separate sky field, or using the image itself to generate a model of the sky, which is then subtracted. The user can select which sky subtraction method to use. Cubes are generated for intensity, variance and mask images. Differential atmospheric refraction is corrected for base on airmass, slicer orientation and wavelength. If a standard star has been observed, flux calibration will be performed as a final step.

The KCWI data reduction pipeline produces three-dimensional flux cubes (α, δ, λ) for each image. In the case of multiple images per field, these data cubes (and their corresponding variance images) need to be rectified and stacked. With bright quasars, the stacking process is relatively straightforward, with the brightest object lined up for all images. Images and stacks are compared to other observations of the field to verify the presence of any background continuum objects and double-check the WCS (World Coordinate System). Images are re-binned to create square pixels.

Because the QSOs in both the QSO1009 and UM287 fields were well separated from the Lyα emission, no QSO subtraction was required.

Adaptive kernel smoothing. After stacking and sky subtraction, the final data cube for each target is run through an adaptive smoothing process[1,2,17,18]. Adaptive kernel smoothing is a process for optimally extracting signal that exists at different spatial scales within an image. This is well suited to CGM/IGM studies, as we expect both large-scale structure and small-scale clumping. In two dimensions, adaptive kernel smoothing begins by smoothing data with the kernel (Gaussian, for example) set at a user-specified minimum scale. Pixels that reach a user-specified signal-to-noise threshold are 'detected' at this scale. Their smoothed values are subtracted from the 'working' image and added to a 'detection' image, and the pixel is masked from future detections so that it can only contribute to further layers via smoothed residuals accumulating on larger scales. The kernel grows in size each iteration until either all of the pixels are masked or a maximum kernel size has been reached, at which point the smoothed background is added to the 'detection' image. The scale at each location in the image is smoothed at its own natural scale. In this way, the scale at each location is the size of the kernel (centred on that pixel) that one would need to sum under to reach the desired signal-to-noise ratio. Thus, an area with bright signal would be minimally smoothed, whereas background areas with little or no signal would be smoothed at larger scales. In three dimensions, this two-dimensional process occurs at each wavelength bin, and a third layer of iteration is added in which the cube is wavelength-binned or smoothed. Starting at the smallest wavelength scale, the two-dimensional process occurs at each layer of the cube. The size of the wavelength kernel is increased and the two-dimensional process is repeated at each layer again, until either all of the voxels are detected or a maximum wavelength scale has been reached. For the data in this paper, a two-dimensional Gaussian kernel was used for spatial smoothing and a one-dimensional boxcar kernel was used for wavelength.

For CSO38B, the signal-to-noise ratio threshold was 3.6. For UM287, the threshold was slightly higher, at 5.1. For both objects, the smoothing window ranges from 1.5 arcsec to 5.8 arcsec, with almost all of the signal in the region smoothed with a kernel size of 1.5–2.6 arcsec. We note that the effective sampling of the CSO38 data is similar to that of UM287 because it was obtained in two orthogonal orientations. The minimum smoothing scale is set to 1.5″ making the datasets essentially equivalent. Also, for the best-fit models, the variations in the velocity map are small at <1.3″ scales, so the sampling difference is not significant.

Velocity, velocity error and dispersion maps. Narrow band flux and intensity-weighted velocity and velocity dispersion maps are created by summing over a velocity window of roughly 1,000 km s^{-1} around the intensity-weighted mean velocity of the Lyα nebula. This procedure is designed to ensure that in each pixel a single gas component dominates so that the velocity mean is not perturbed by multiple superposed components. Given the high signal-to-noise ratio, the mean velocity error is typically less than 10–15 km s^{-1}. The outer regions of the images are trimmed to exclude regions with intensity less than 7 kLU (CSO38B) or 4 kLU (UM287), and velocity error greater than 50 km s^{-1}. The black regions in all the maps (see Figs. 2, 4 and so on) are below either these thresholds or below the smoothing threshold. Because both objects are quite bright, and fall off in intensity quite rapidly at their boundaries, the area fitted and the resulting best-fit parameters and χ^2 are only weakly dependent on this trimming threshold.

We have examined the effect of a higher signal-to-noise ratio threshold on both objects. We doubled the signal-to-noise ratio threshold from 7 kLU to 14 kLU for CSO38B. We show in Supplementary Fig. 9a that the dramatic drop in AIC from Model 2 to Model 3a(i) is unchanged. For UM287, we perform the same experiment, doubling the signal-to-noise threshold from 4 kLU to 8 kLU. Supplementary Fig. 9b shows that the AIC drop on reaching Model 3c(i) is essentially the same. The conclusions of the paper are thus not sensitive to small changes in the signal-to-noise threshold and are not unduly influenced by the lowest signal-to-noise data.

Velocity error maps are generated from signal-to-noise ratio cubes that are an output of the smoothing algorithm. Examples are shown in Supplementary Fig. 7, along with a more detailed discussion on sources of errors in the Supplementary Notes. In brief, we use the root-mean-square velocity residual as a conservative estimate, given that the statistical error and the sky subtraction error are found to be negligible by comparison.

Protogalaxy numerical simulation. Our cosmological simulations use the hydro-gravitational code ART[21–23], which uses adaptive mesh refinement to follow the Eulerian gas dynamics. The code implements sub-grid models of the key physical processes relevant for galaxy formation. These include gas cooling by atomic hydrogen and helium, molecular hydrogen and metals, and photo-ionization heating by an ultraviolet background with partial self-shielding. Star formation is stochastic in cells with gas temperature $T<10^4$ K and volume number densities $n_H>1$ cm^{-3}, at a rate consistent with the Kennicutt–Schmidt law[24]. Stellar mass loss and metal enrichment of the interstellar medium are included. Feedback from stellar winds and supernovae is implemented by injecting thermal energy to the neighbouring gas at a constant rate. Radiative stellar feedback is implemented at a moderate level, with very little infrared trapping[12,25].

The cosmological model adopted in the simulation is the standard cold dark matter model with the WMAP5 cosmological parameters ($\Omega_m=0.27$, $\Lambda=0.73$, $\Omega_b=0.045$, $h=0.7$, $\sigma_8=0.82$)[26]. Individual haloes were selected at $z=1$ from an N-body dark-matter-only simulation of a large cosmological box. Each halo and its environment were re-simulated at higher resolution with gas and the associated baryonic processes. The dark matter in each halo, out to a few virial radii, is typically represented by about 5×10^7 particles of mass $8.3\times10^4 M_\odot$ each. The particles representing stars have a minimum mass of $10^3 M_\odot$. The adaptive mesh refinement cells in the dense regions are refined to a minimum size in the range 17.5–35 pc at all times. The adaptive refinement algorithm is such that a cell is divided into eight cells once it contains a mass in stars and dark matter of more than $2\times10^5 M_\odot$, or a gas mass larger than $1.5\times10^6 M_\odot$. The force resolution is one to two grid cells of the maximum resolution. Artificial fragmentation on the cell size is prevented by introducing a pressure floor, which ensures that the Jeans scale is resolved by at least seven cells[27].

VELA07 and conversion into observed quantities. The simulated galaxy analysed here is VELA07 at $z=2$, referring to gas of $T<5\times10^4$ K. This galaxy at $z=2$ has a virial mass of $0.9\times10^{12} M_\odot$, corresponding to a virial radius of 104 kpc, Its stellar mass is $5.7\times10^{10} M_\odot$ with an effective radius of 2.8 kpc. In order to compare to more massive galaxies all quantities should be scaled up.

The VELA07 simulation snapshot consists of a list of cells with gas density, temperature, velocity and cell size. From this list we create an observed intensity cube assuming that the gas is ionized by the nearby QSO and is emitting recombination Lyα in ionization equilibrium. The fundamental equation for the intensity/velocity cube for a given orientation (expressed in LU) is, for simulation cell i:

$$I(x_i, y_i, v_i) = I(x_i, y_i, v_i) + \left[\frac{\alpha f_i}{4\pi(1+z)^3}\right] n_i^2 l_i \left(\frac{l_i}{L}\right)^2$$

where x_i and y_i are the projected position, v_i the line-of-sight velocity, n_i the gas density, l_i the cell size, L the pixel size in the intensity cube, and $f_i<1$ corrects for the ionization fraction at high densities ($f_i \cong 1$ for all but the highest densities). For simplicity we assume that the gas is at a fixed temperature ($T=20{,}000$ K). The intensity/velocity cube for each orientation is used to generate an intensity-weighted mean velocity map. Radiative transfer effects are discussed below.

The maps shown in Figs. 2 and 4 also include the most prominent star-forming regions in the simulation. Source A, at the maximum of the intensity and gas

column density profile, is a galaxy with stellar mass $6.3\times10^{10}M_{\odot}$, star-formation rate $27M_{\odot}$ yr^{-1}, and mass-weighted stellar age of 1.0 Gyr. Source B, offset from the centre and not present in Fig. 4, is an object with stellar mass $8.5\times10^{8}M_{\odot}$, star-formation rate $0.26M_{\odot}$ yr^{-1}, and mass-weighted stellar age of 1.2 Gyr. Finally, object C, also offset, has stellar mass $7.3\times10^{8}M_{\odot}$, star-formation rate $0.21M_{\odot}$ yr^{-1}, and mass-weighted stellar age of 1.4 Gyr.

We also analysed two other simulated galaxies, VELA20 and VELA21. The column density distributions are shown in Supplementary Fig. 10. The dependence of AIC on the MFI model is shown in Supplementary Fig. 11 for three different line-of-sight directions for all three VELA-simulated galaxies. We confirm that MFI models provide a far better representation for all three simulated galaxies by finding a pronounced drop in AIC as we pass from Model 1 to Models 3 and 4 in each case and for all lines of sight.

Radiative transfer effects. We have assumed that the velocity maps correctly represent the underlying gas kinematics. As in ref. [1], we do not include any radiative transfer effects on the escape of Lyα. We note that proximate QSO illumination leads to high ionization ratios and relatively low H I column densities. For CSO38B, we estimate that at a proper distance of 100 pkpc the ionization rate $\Gamma=2\times10^{-8}$ s^{-1}, which for a maximum column number density of $N_{\rm H}=10^{21}$ cm^{-2}, slab thickness of 3 kpc, and gas temperature $T=2\times10^{4}$ K, results in a neutral hydrogen column density of $N_{\rm H\,I}=4\times10^{14}$ cm^{-2}. For UM287 this becomes $N_{\rm H\,I}=10^{15}$ cm^{-2}. Even lower column densities are likely since the gas temperature is predicted to be higher ($T>10^{5}$ K) owing to the photoionization heating. The resulting optical depths in the line centre are low, $\tau\approx2$–20. Since the Lyα emission is generated by recombination in the ionized gas, it will be generated with the line centre reflecting the local velocity of the gas. It is well known that the velocity centre of the emerging Lyα line from a slab of gas at a fixed velocity is centred on that velocity[28–30]. Therefore the principal question to be addressed is whether a substantial column density of neutral hydrogen is present along the line of sight that has a different velocity. In the case of the MFI model, the gas is confined to a relatively thin slab, with a single velocity associated with each radial/azimuthal postion. Thus, whereas the linewidth could be increased (or even doubled) depending on the optical depth, the line centre should accurately reflect the local velocity by construction. In the case of the VELA simulations, we can check by estimating the three-dimensional distribution of H I. We used CLOUDY[31] to estimate the dependence of the local gas temperature on the gas density. We then calculate the local H I column density in each voxel. For each of three different projections we then calculate the emissivity-weighted velocity and the N(H I)-weighted velocity, and compare them. They are quite close, with a slope near unity and a small dispersion of about 10 km s^{-1}. Thus, even in the presence of some photon diffusion the local velocity measurement should be accurate.

MFI protogalaxy criteria. We proposed a set of criteria to evaluate whether a Lyα nebula was consistent with the previously termed 'protogalactic disk'[2], presented as a Supplementary Note. Here, we revise these, recognizing the characteristics of an MFI protogalaxy and then evaluate the two objects in light of the revised criteria.

Revised MFI protogalaxy criteria.

1. Higher intensity located approximately symmetrically around one-dimensional velocity centre; relatively uniform intensity with clear intensity break at edges;
2. Two-dimensional velocity and intensity distribution consistent with a disk and multi-filament radial flow in an NFW halo with minimal residuals;
3. Evidence for one or more filaments with low velocity gradient and possibly lower-velocity dispersion aligned with inferred radial flow direction(s);
4. Velocity gradients transverse to rotation-induced velocity shear;
5. Star formation near centre of disk with radial mass flux onto galaxy consistent with star-formation rate;
6. Object is separated from illuminating QSO and does not appear to be part of interaction producing the QSO.

We summarize the two objects in the context of these revised criteria in Supplementary Table 2.

MFI models. Four model classes, each successively more complex, were used to fit the mean velocity maps. A summary of the models is provided in Supplementary Table 3.

Model 1. Simple equilibrium rotation. Simulations show a transition from a plane for the outer halo (>0.3$r_{\rm v}$, where $r_{\rm v}$ is the virial radius) to a somewhat modified plane for the inner halo (<0.3$r_{\rm v}$)[4]. The emission we observe is largely within 0.5$r_{\rm v}$, so for simplicity we retain a single plane. This model[1,2] thus assumes that the emitting gas lies in a flattened disk that is rotating in Keplerian equilibrium in an NFW dark matter halo. The halo is determined by the halo mass and concentration. In addition, the disk inclination, position angle, and velocity centre are fitted as well. The object centre is fixed at the centre of light. Allowing the object centre to be fitted as well does not change any conclusions. Halo concentration is not well constrained, and the fit is limited to $0<\log c<1$. Disk thickness does not enter into the kinematic model. There are five free parameters to fit.

There is an ambiguity in the disk orientation. Only the angular momentum projected in the plane of the sky can be measured. The angular momentum vector can be oriented toward the observer, or away. For pure rotation this does not matter, but when radial flow is added the sign of the flow (inflow versus outflow) is reversed in the two cases.

Model 2. Rotation plus radial flow. This model adds a radial flow component to the disk rotation velocity field of Model 1. Examination of the VELA07 simulation protogalaxy shows that the radial component of the flow inside the virial radius decreases approximately linearly with radius. We therefore assume that the radial flow velocity is linearly proportional to radius. The amplitude quoted is the radial velocity at the virial radius of the halo. In all models we assume that the radial flow is in the same plane as the rotation, and constant in azimuth. This adds one additional free parameter, totalling six. We also resolve the orientation ambiguity by assuming there is net radial inflow. In all cases the inferred inflow directions (in Models 3 and 4) are consistent with filamentary extensions, validating this approach.

In some simulations[32] the radial velocity is constant with radius for $r>0.3r_{\rm V}$. Note that for all three galaxies there is no velocity information for $r>0.5r_{\rm V}$. We considered two additional radial velocity dependencies for Models 2 to 4. The first is a simple constant independent of radius, and the second is constant for $r>0.3r_{\rm V}$ and linearly varying with radius for $r\leq0.3r_{\rm V}$. In both cases these variations produced somewhat poorer fits to the VELA07 simulation, CSO38B and UM287. Therefore for this investigation we retain the linear dependence at all radii as the baseline model. As the gas circularizes later in the evolution of the protogalaxy, the radial component should decrease or remain constant, depending on the balance of gravitational and dissipational forces.

Model 3a. MFI, one mode. Examination of Fig. 1 shows that in the simulated galaxy the radial flow amplitude varies with azimuth. This is to be expected as gas is inflowing preferentially along filaments. In this family of models we allow the radial flow to be azimuthally modulated by sinusoids. For Model 3a, the azimuthal function is a single sinusoid with one cycle per rotation. This component is added to the constant radial component of Model 2. See Supplementary Table 3 for the equation. For Model 3a(i), the azimuthal phase is fixed with radius. Model 3a(i) adds two additional parameters, the amplitude and the aziumuthal phase of the modulation, for a total of eight fitting parameters. For Model 3a(ii), the azimuthal phase is permitted to vary linearly with radius, creating a spiral phase, and adding one additional parameter, for a total of nine. Note that radial flow can be inward or outward. Inward radial flow along the disk plane seems natural, while outflow does not. Examination of Fig. 1 shows azimuthal zones where radial outflow is occuring, presumably from inflowing gas that does not completely circularize before overshooting with some outward component. Outflow due to winds from star formation and active galactic nucleus activity would be expected to be perpendicular to the disk, although when the disk is inclined could appear to have a component parallel to the disk when radiative transfer affects are included. Wind outflows are not included in the model.

Roughly speaking, Model 3a provides a good representation of a system in which a single filament is providing the bulk of the accretion inflow. Model 3b allows for two and Model 3c for three. In the case of Model 3c the relative importance and azimuthal zone of each filament is determined by the free parameters, and one filament may still dominate. While the three-filament configuration is often seen to be the default[4,5,19], the number of prominent streams may be dependent on mass and redshift[33]. One of our objectives in this work is to test for the presence of multiple filaments by investigating the dependence of the fit quality on the number of modes.

Model 3b. MFI, two modes. To Model 3a we add a second modulation, with two cycles per rotation. This adds to Model 3b(i) two more parameters, giving a total of ten, and for Model 3b(ii) the number of parameters is now 11.

Model 3c. MFI, three modes. To Model 3b we add a third modulation, with three cycles per rotation. This adds to Model 3c(i) two more parameters, giving a total of 12, and for Model 3b(ii) the number of parameters is now 13.

Model 4. MFI, three modes, azimuthal velocity modulation. For Models 1 to 3 we have assumed that the azimuthal velocity at a given radius is simply determined by the enclosed dark-matter mass. Examination of Fig. 1 also shows azimuthal variations of the azimuthal velocity that are correlated with the azimuthal variations in the radial velocity. We allow for this by adding one more parameter, positive or negative, which when multiplied by the total radial velocity field, is added to the azimuthal velocity field. This results in 14 free parameters.

Model fitting. Models are fitted by minimizing the total χ^2 calculated from the difference between the data and velocity model map. We use a Powell minimization routine[34] to find the minimum. With many parameters we find that starting the minimization routine with different initial parameter values can lead to different

local minima. We therefor 'anneal' by repeating the minimization search with randomly chosen initial parameters. We note that the minimum-χ^2 models all have comparable model parameters and in particular similar MFI components. This is illustrated in Supplementary Fig. 8. In this case, the three minimum-χ^2 fits to Model 4, UM287 are shown. Iterations 15, 0 and 1 have AIC values of 351, 364 and 379, yet have very comparable MFI components. Thus, the MFI modes are not suppressed in some of the local minima, and are similar in model fits with similarly low-χ^2. Model parameter errors are determined in the usual fashion by fixing the parameter of interest and allowing the remaining parameters to vary. Error ranges for the derived parameters (such as mass flux) are obtained during the above error determination. For each parameter's 1σ limits we derive the corresponding derived parameter values. Then the maximum and minimum of the ensemble over all the parameters gives the 1σ range of the derived parameter.

Akaike Information Criterion. We use the AIC[13] to judge whether a model with a larger number of parameters is a better representation of the data than a model with fewer parameters and larger χ^2. For small sample size it is:

$$\mathrm{AIC} = \chi^2 + 2p + \frac{2p(p+1)}{N-p-1}$$

Here p is the number of parameters and N is the number of degrees of freedom. The minimum AIC is the most likely model. The probability that Model i minimizes the information loss given the minimum AIC model is $\mathrm{P(AIC}_i) = \exp((\mathrm{AIC}_{\mathrm{min}} - \mathrm{AIC}_i)/2)$. This is the probability tabulated in Supplementary Tables 4, 2 and 6. To be conservative we calculate the χ^2 with the number of degrees of freedom determined by the seeing disk and smoothing algorithm and not simply by the number of pixels, and rather than using the formal velocity error, which is quite small (about 10–15 km s^{-1}), we use the minimum root-mean-square residual velocity, which is typically around 70 km s^{-1} (except for the VELA07 simulation, for which it is around 50 km s^{-1}). We have also evaluated the Bayesian Information Criteria (BIC)[35], given by:

$$\mathrm{BIC} = \chi^2 + p\ \log(N)$$

These are tabulated in Supplementary Table 6, and show a very similar behaviour to that of the AIC. The tabulated BIC probabilities assume that the models have equal prior probability.

Physical parameter derivation. Baryonic mass, angular momentum, and radial mass flux require an estimate of the gas column density. As we have done in earlier work[1,2], we assume that the gas is fully ionized by the QSO and situated in a roughly planar disk. The disk thickness t and gas clumping factor C are unknowns. Given this assumption, the intensity (in units of kLU) is approximately

$$I = 250\ N_{21}^2 t_3^{-1} C$$

where as usual at $\lambda = 4{,}000$ Å

$$1\ \ \mathrm{kLU} = 10^3\ \ \mathrm{ph\ cm^{-2}\ \ s^{-1}\ \ sr^{-1}} \approx 10^{-19}\ \ \mathrm{erg\ \ cm^{-2}\ \ s^{-1}\ \ arcsec^{-1}}$$

We assume that the disk thickness is 3 kpc ($t_3 = 1$) and clumping factor $C = 1$. The radial mass flux is given by

$$2\pi \frac{\mathrm{d}\dot{M}}{\mathrm{d}\phi}(r,\phi) = ArN_{\mathrm{H}}(r,\phi)\, v_{\mathrm{r}}(r,\phi)$$

Detailed tabulations of the best-fit parameters and derived physical parameters for each model are given in Supplementary Tables 4–6. Parameter error ranges for the adopted models are given in Supplementary Table 7.

Detailed maps in observed and face-on frame. We have generated a series of maps in the observed and inferred face-on frames in order to gain more insight into the implications of the MFI model fits and derived velocity fields. These are shown for the best-fit models for the VELA07 simulation (Supplementary Fig. 3), CSO38B (Supplementary Fig. 5) and UM287 (Supplementary Fig. 6). These maps show azimuthal and radial velocity components, radial mass flux, inferred column density and velocity field maps. We note in particular that in each case the direction of the principal radial inflow aligns with directions manifesting filamentary extensions. The flow direction is such that in each case gas will be brought to the central galaxy to fuel on-going star formation.

Continuum objects in the field and impact on conclusions. CSO38B has four continuum sources detected in or nearby the nebula (Fig. 2). We present a fully detailed description of these sources in the Supplementary Notes. Since galaxies are present in the nebula, we need to address three questions: (1) How much of the emission is produced by the halo of the galaxy itself? (2) Do outflows from supergalactic winds have any impact on the kinematics or the conclusions? (3) Are there tidal interactions which affect the kinematics and the conclusions of this paper?

(1) Halo emission. The surface brightness is about ten times higher than the brightest Lyα halo emission seen around star-forming galaxies at slightly higher redshift[36], when corrected for surface brightness dimming. We conclude that the Lyα emission is powered mostly by QSO-illuminated fluorescence rather than by the star-forming galaxy. The emission is brightest around BX173 because there the gas column density is highest.

(2) Emission measure, kinetic energy flux and kinematic signature. We argue here that, first, the emission measure in the wind is insufficient to produce a substantial fluorescent signal, second, that the kinetic energy flux is insufficient to produce a large kinematic signature except very close to the galaxy, and third, that a kinematic signature is not observed, except for increased velocity dispersion near the galaxy.

First, we can estimate the emission measure by assuming isotropic flow into Ω (in units of steradians) and an entrained cold-gas mass flow rate that is approximately equal to the star-formation rate[37]. We find that

$$\mathrm{EM\,(cm^{-5})} \approx 2\times 10^{16} \left(\frac{\dot{M}_{\mathrm{w}}}{10 M_{\odot}\ \mathrm{yr}^{-1}}\right)^2 \left(\frac{b}{10\ \mathrm{kpc}}\right)^{-3} \left(\frac{v_w}{500\ \mathrm{km\ s}^{-1}}\right)^{-2} \left(\frac{\Omega}{4\pi}\right)^{-2} C$$

where $\dot{M}_{\mathrm{w}}$ is the wind cold-gas mass flux, b is the projected impact parameter ($> b_{\mathrm{min}} \approx 3$ kpc the typical size of a starburst wind base), v_w is the wind velocity, and C is the clumping factor. This is about a factor of 10,000 below the observed emission measure for $C = 1$. The radial outward flow leads to a steeply falling density profile, and the density square dependence produces a very low emission measure even if the clumping factor were much greater than unity. Note that while external fluorescent illumination is probably undetectable, without an ionizing QSO nearby, Lyα emission produced in the galaxy can encounter a large optical depth and therefore will diffuse out, producing an extended halo, as is observed in star-forming galaxies[36,38]. As we noted above, the surface brightness of this halo is much lower than we observe.

Second, we attempt to estimate the impact of the wind kinetic energy flux on the motions of cold gas in the galaxy. It is expected that the supergalactic winds in average-mass galaxies with established disks will form a bipolar outflow along the angular momentum axis of the star-forming galaxy, as this is the path of least resistance. The emission nebulae produced by these supergalactic winds are typically confined within a few kiloparsecs. To be conservative, we can assume that an areal fraction $f_{\mathrm{areal}} \approx \frac{2\pi rt}{(4\pi r^2)}$ at radius r of agas sheet of thickness t intercepts what we will assume is an isotropic kinetic energy flux[37] of $\dot{E}_w \approx 2\times 10^{41} \dot{M}_{\star}$, where $\dot{M}_{\star}$ is the stellar flux, operating for a dynamical time for that radius (since the gas is constantly being replenished by ongoing accretion). For BX173 this gives a total kinetic energy of about 10^{57} ergs. Very conservatively assuming this all goes into random velocity of the cold gas, the (one-dimensional) velocity dispersion of the gas will be $\sigma_{\mathrm{v}} \approx 23$ km s^{-1}, a relatively small impact. Other than large-scale shocks moving radially outward, there is no clear mechanism by which galactic winds can substantially perturb the velocity field of the large cold gas reserve. We do note that the velocity dispersion is high near the galaxy. This may be due to unresolved rotation or turbulent motion, partially due to the injection of wind energy.

Third, other than the increase in the velocity dispersion near the galaxy, there is no kinematic signature of a large-scale galactic wind. There is no large, bi-conical morphology with large velocity offsets. There is no detected radial outflow centred on BX173.

These conclusions hold equally for galaxy MD23. Moreover, excluding the region near MD23 from the fit does not change the conclusions of the fit. This is because the best-fit model, Model 3a(i), does not do a good job in the region near MD23 (Fig. 3, Supplementary Fig. 2)

(3) Tidal interactions. Are there tidal interactions between the galaxies BX173 and MD23? Can the presence of MD23 approximately 40 kpc away (in projection) affect the kinematics of the gaseous nebula? Given the relative velocity of the two galaxies, the projected distance, and assuming that MD23 is at the centre of a dark matter subhalo with ten times the stellar mass of MD23, we can estimate that the velocity gradient induced by tidal forces will be at most 1 km s^{-1} kpc^{-1}. The gradient observed in the central part of the nebula is about 10 km s^{-1} kpc^{-1}. Also, as we discuss below, the morphology of the nebula does not resemble that of nearby interacting galaxies with tidal features.

UM287 shows continuum sources in the brightest part of the nebula[1]. A full description of these sources is presented in our Supplementary Notes. However, the discussion above concerning haloes, winds and tidal interactions also applies to this system.

Smooth versus clumpy accretion in a preferred plane. The accretion of cold gas along streams, the scenario we are addressing in this paper, includes the rapid accretion of gas along a plane of satellites. Phenomena previously described that include coplanar streams[4,5] and extended rings[4] are examples showing that cold streams define a preferred plane (both in the Horizon-MareNostrum RAMSES simulation[39] and in the VELA simulation used here). It has always been argued and shown in the simulations[19] that the cold streams are partly made of smooth gas and partly clumpy, including all the merging galaxies. So the stellar and gas accretion of satellites is part of the cold spiral inflow phenomenon.

Alternative models. We must consider whether alternative models can explain the observed intensity and velocity maps. In particular, both systems reside in the neighbourhood of a luminous QSO. We provide an additional note on the impact of selecting such objects in the Supplementary Notes. The QSO is probably a result of a complex interaction or merger, and it is conceivable that the gas nebulae were created as a byproduct of this interaction.

For CSO38, the projected distance between CSO38 and CSO38B is 120 pkpc. There is no morphological resemblance to nearby interacting systems such as NGC4038/39[40] and the projected distance is probably too large for CSO38B to be an interaction byproduct. As we discussed above, the interaction of BX173 and MD23 is unlikely to affect the kinematics very much.

For UM287 we previously considered three classes of alternative models to a cold-flow accretion scenario[1]. We review these in light of the higher-resolution KCWI data without changing our previous conclusions.

Scenario one is that the nebula is created by an interaction involving the neighbouring quasar (QSO B), leading to a merging disk and tidal tails fluoresced by QSO A. The arguments against this have not changed: no Lyα emission or complex kinematics near QSO B, and no evidence of long, thin, curved tidal tails with a continuous velocity shear and fall-back gradient[40].

Scenario two holds that the bright part of the filament is part of a merging disk hosting QSO A or the tidal tail, and that the faint filament is part of the tidal tail. The complex kinematics revealed by KCWI are even less consistent with that expected for merging rotating disks, although all possible scenarios cannot be evaluated. The filament does not exhibit the curvature in velocity–position space of a tidal tail[1,40]. The bright nebula is tangential to QSO A rather than centred on it, and the higher resolution of KCWI does not reveal any extended emission centred on QSO A from the interacting host galaxy forming QSO A. A tidal tail would extend radially outward and then curve tangentially in the plane of the merging disk and QSO A, and would probably show a large velocity gradient and a discontinuity at the tail–disk interface. The filament is also wider than expected (about 60 pkpc versus 10–20 pkpc).

Scenario three posits a separate interacting system that is not responsible for QSO A or B, but this is also ruled out by the same arguments as above. We note, however, that QSO A could have been produced in its own host galaxy by the tidal forces and radial flows owing to the influence of the nearby forming protogalaxy and associated subhalo that we are observing.

Data availability

KCWI data on CSO38 and UM287 is publicly available. Data on UM287 will be available 18 months after the observation in Oct 2017. The data that support the plots within this paper and other findings of this study are available from the corresponding author upon reasonable request.

Code availability

KCWI pipeline code is available on the W. M. Keck Observatory website.

Received: 7 March 2019; Accepted: 25 April 2019;
Published online: 1 July 2019

References

1. Martin, D. C. et al. A giant protogalactic disk linked to the cosmic web. *Nature* **524**, 192 (2015).
2. Martin, D. C. et al. A newly forming cold flow protogalactic disk, a signature of cold accretion from the cosmic web. *Astrophys. J.* **824**, L5 (2016).
3. Morrissey, P. et al. The Keck Cosmic Web Imager Integral Field Spectrograph. *Astrophys. J.* **864**, 93 (2018).
4. Danovich, M. et al. Four phases of angular-momentum buildup in high- *z* galaxies: from cosmic-web streams through an extended ring to disc and bulge. *Mon. Not. R. Astron. Soc.* **449**, 2087–2111 (2015).
5. Danovich, M., Dekel, A., Hahn, O. & Teyssier, R. Coplanar streams, pancakes and angular-momentum exchange in high- *z* disc galaxies. *Astrophys. J.* **422**, 1732–1749 (2012).
6. Stewart, K. et al. Orbiting circumgalactic gas as a signature of cosmological accretion. *Astrophys. J.* **738**, 39 (2011).
7. Stewart, K. R. et al. Angular momentum acquisition in galaxy halos. *Astrophys. J.* **769**, 74 (2013).
8. Arrigoni-Battaia, F. et al. Inspiraling halo accretion mapped in Lyα emission around a $z \sim 3$ quasar. *Mon. Not. R. Astron. Soc.* **473**, 3907–3940 (2017).
9. Vanzella, E. et al. Illuminating gas inflows/outflows in the MUSE deepest fields: Lyα nebulae around forming galaxies at $z \simeq 3.3$.*Mon. Not. R. Astron. Soc.* **465**, 3803–3816 (2017).
10. Navarro, J. F., Frenk, C. S. & White, S. D. M. A universal density profile from hierarchical clustering. *Astrophys. J.* **490**, 493–508 (1997).
11. Zolotov, A. et al. Compaction and quenching of high-*z* galaxies in cosmological simulations: blue and red nuggets. *Mon. Not. R. Astron. Soc.* **450**, 2327–2353 (2015).
12. Ceverino, D. et al. Radiative feedback and the low efficiency of galaxy formation in low-mass haloes at high redshift. *Mon. Not. R. Astron. Soc.* **442**, 1545–1559 (2014).
13. Akaike, H. A new look at the statistical model identification. *IEEE Trans. Autom. Control* **19**, 716–723 (1974).
14. Cantalupo, S., Arrigoni-Battaia, F., Prochaska, J. X., Hennawi, J. F. & Madau, P. A cosmic web filament revealed in Lyman-α emission around a luminous high-redshift quasar. *Nature* **506**, 63–66 (2014).
15. Trainor, R. & Steidel, C. C. Constraints on hyperluminous QSO lifetimes via fluorescent Lyα emitters at $z \simeq 2.7$. *Astrophys. J.* **775**, L3 (2013).
16. Trainor, R. F. & Steidel, C. C. The halo masses and galaxy environments of hyperluminous QSOs at $z \simeq 2.7$ in the Keck Baryonic Structure Survey. *Astrophys. J.* **752**, 39–51 (2012).
17. Martin, D. C. et al. IGM emission observations with the Cosmic Web Imager: I. The circum-QSO medium of QSO 1549+19, and evidence for a filamentary gas inflow. *Astrophys. J.* **786**, 106–131 (2014).
18. Martin, D. C. et al. IGM emission observations with the Cosmic Web Imager: II. Discovery of extended, kinematically-linked emission around SSA22 Lymanα Blob 2. *Astrophys. J.* **786**, 107–135 (2014).
19. Dekel, A. et al. Cold streams in early massive hot haloes as the main mode of galaxy formation. *Nature* **457**, 451–454 (2009).
20. Dekel, A. & Birnboim, Y. Galaxy bimodality due to cold flows and shock heating. *Mon. Not. R. Astron. Soc.* **368**, 2–20 (2006).
21. Ceverino, D. & Klypin, A. The role of stellar feedback in the formation of galaxies. *Astrophys. J.* **695**, 292–309 (2009).
22. Kravtsov, A. V. On the origin of the global Schmidt law of star formation. *Astrophys. J.* **590**, L1–L4 (2003).
23. Kravtsov, A. V., Klypin, A. A. & Khokhlov, A. M. Adaptive Refinement Tree: a new high-resolution *N*-body code for cosmological simulations. *Astrophys. J. Suppl.* **111**, 73–94 (1997).
24. Kennicutt, R. C. J. The global Schmidt law in star-forming galaxies. *Astrophys. J.* **498**, 541–552 (1998).
25. Dekel, A. & Krumholz, M. R. Steady outflows in giant clumps of high-*z* disc galaxies during migration and growth by accretion. *Mon. Not. R. Astron. Soc.* **432**, 455–467 (2013).
26. Komatsu, E. et al. Five-year Wilkinson microwave anisotropy probeobservations: cosmological interpretation. *Astrophys. J.* **Suppl. 180**, 330–376 (2009).
27. Ceverino, D., Dekel, A. & Bournaud, F. High-redshift clumpy discs and bulges in cosmological simulations. *Mon. Not. R. Astron. Soc.* **404**, 2151–2169 (2010).
28. Neufeld, D. A. The transfer of resonance-line radiation in static astrophysical media. *Astrophys. J.* **350**, 216 (1990).
29. Verhamme, A., Schaerer, D. & Maselli, A. 3D Lyα radiation transfer. *Astron. Astrophys.* **460**, 397–413 (2006).
30. Zheng, Z. & Miralda-Escudé, J. Monte Carlo simulation of Lyα scattering and application to damped Lyα systems. *Astrophys. J.* **578**, 33–42 (2002).
31. Ferland, G. J., Korista, K. T., Verner, D. A., Ferguson, J. W., Kingdon, J. B. & Verner, E. M. CLOUDY 90: numerical simulation of plasmas and their spectra. *Publ. Astron. Soc. Pac.* **110**, 761–778 (1998).
32. Goerdt, T. & Ceverino, D. Inflow velocities of cold flows streaming into massive galaxies at high redshifts. *Mon. Not. R. Astron. Soc.* **450**, 3359–3370 (2015).
33. Cen, R. Evolution of cold streams and the emergence of the Hubble sequence. *Astrophys. J.* **789**, L21 (2014).
34. Powell, M. J. D. An efficient method for finding the minimum of a function of several variables without calculating derivatives. *Comput. J.* **7**, 155–162 (1964).
35. Schwarz, G. Estimating the dimension of a model. *Ann. Stat.* **6**, 461–464 (1978).
36. Wisotzki, L. et al. Extended Lyman α haloes around individual high-redshift galaxies revealed by MUSE. *Astron. Astrophys.* **587**, A98 (2016).
37. Heckman, T. M., Armus, L. & Miley, G. K. On the nature and implications of starburst-driven galactic superwinds. *Astrophys. J. Suppl.* **74**, 833–868 (1990).
38. Steidel, C. C. et al. Diffuse Lyα emitting halos: a generic property of high-redshift star-forming galaxies. *Astrophys. J.* **736**, 160–177 (2011).
39. Ocvirk, P., Pichon, C. & Teyssier, R. Bimodal gas accretion in the Horizon-Mare Nostrum galaxy formation simulation. *Mon. Not. R. Astron. Soc* **390**, 1326–1338 (2008).
40. Hibbard, J. E., van der Hulst, J. M., Barnes, J. E. & Rich, R. M. High-resolution H [CSC]i[/CSC] mapping of NGC 4038/39 ("The Antennae") and its tidal dwarf galaxy candidates. *Astron. J.* **122**, 2969–2992 (2001).

Acknowledgements

This work was supported by the National Science Foundation, the W. M. Keck Observatory and the California Institute of Technology. The VELA simulations were performed at NASA Advanced Supercomputing at NASA Ames Research Center. D.C. is funded by the ERC Advanced Grant, STARLIGHT: Formation of the First Stars (project number 339177).

Author contributions

D.C.M. is the Principal Investigator of KCWI, performed the analysis of the simulated galaxy, data and MFI models, and was principal author on the paper. D.O. and D.C.M. led the observations of UM287 and CSO 38. D.O. and M.M. reduced the data. D.O., M.M. and E.H. contributed to the paper writing. P.M., M.M., D.C.M., J.D.N., D.O. and A.M. designed, constructed and operated KCWI. J.D.N., M.M. and D.C.M. developed the KCWI data pipeline and produced the final data cubes. D.C. developed the VELA simulations. A.D. and S.L. provided the simulated galaxy VELA07 and contributed to the writing of the paper. D.C. and J.P. contributed the cosmological simulation. C.S., R.T., S.C. and J.X.P. contributed to the development of KCWI, to Keck data for the two protogalaxies, and to the editing of the paper. L.R. made major contributions to KCWI commissioning and participated in the observations of CSO 38.

Competing interests

The authors declare no competing interests.

Additional information

Supplementary information is available for this paper at https://doi.org/10.1038/s41550-019-0791-2.

Reprints and permissions information is available at www.nature.com/reprints.

Correspondence and requests for materials should be addressed to D.C.M.

Publisher's note: Springer Nature remains neutral with regard to jurisdictional claims in published maps and institutional affiliations.